Journal of Materials Chemistry A

ROYAL SOCIETY OF CHEMISTRY

PAPER

View Article Online
View Journal | View Issue

Cite this: *J. Mater. Chem. A*, 2022, **10**, 25347

A MOF-based electronic nose for carbon dioxide sensing with enhanced affinity and selectivity by ionic-liquid embedment†

Peng Qin, Salih Okur, Yunzhe Jiang and Lars Heinke *

The unequivocal detection of CO_2 is important in many situations, like in the living environment, plant cultivation and the conservation of cultural relics and archives. Due to their large specific surface areas and highly ordered and tunable structures, metal–organic frameworks (MOFs) have the potential to improve CO_2 sensing, however, they often suffer from low CO_2 affinity and selectivity. Ionic liquids (ILs) have high CO_2 affinity, but their performance in sensors is hampered by their nonporous, liquid form. Here, we present a low-cost and portable CO_2 sensor system based on an array of gravimetric sensors made of MOF films with embedded ILs in the pores. The array is composed of MOF films of two different structures, which are HKUST-1 and UiO-66, filled with 3 different types of ILs and 2 different pore-filling levels, resulting in an array of up to 14 different sensors. We show that the different combinations of IL and MOF result in different affinities for CO_2 and other analytes. With the help of machine learning using a neural network, the sensor array was used to quantify the CO_2 concentration as well as to distinguish CO_2 from other gases and vapors, like nitrogen, ethanol, methanol and water, and to distinguish certain binary mixtures. While the MOF-sensor array without IL achieves only a small accuracy for determining the CO_2 concentration, the IL@MOF sensor array can accurately classify the gas types (98% accuracy) in mixed gas atmospheres of unknown composition and concentration as well as can determine the CO_2 gas concentration with an average error of only 2.7%. Using only MOFs with a pronounced chemical stability (like UiO-66) in the sensor array also allows the detection and identification of CO_2 in a humid atmosphere. Moreover, the presented sensor system has very high sensitivity with a CO_2 limit of detection below 100 ppm, which is four times smaller than the CO_2 concentration in air. This work shows the unprecedented performance of the sensor arrays of MOFs with embedded ILs, referred to as IL@MOF-electronic nose (IL@MOF-e-nose), for sensing the composition and concentration of CO_2 gas mixtures.

Received 10th August 2022
Accepted 27th October 2022

DOI: 10.1039/d2ta06324g

rsc.li/materials-a

Introduction

Carbon dioxide is an essential component of the atmosphere, a frequent product of life activities and industrial processes as well as the major culprit of the global greenhouse effect.[1] Apart from the climate damage, high CO_2 levels can have a variety of effects and can be harmful to human health. When the concentration remains at 0.3% or higher for a long time, people may experience significant headaches, and people will feel dizzy at CO_2 concentrations of 4–5%.[2] CO_2 concentrations of at least 9% for more than 5 minutes may cause the death of humans.[3] In indoor situations, the main CO_2 sources are exhaled breath and open fires, *e.g.* from fireplaces, candles and gas cookers. Especially in relatively sealed rooms (*e.g.* air-conditioned rooms without ventilation and air exchange), the CO_2 concentration gradually increases and can quickly reach critical values. There, the CO_2 detection is vital. In addition to the indoor applications, carbon dioxide sensing is critical for many different industrial applications, including landfills,[4] horticulture,[5] controlled atmosphere storage and packaging[6] and metal treatment.[7]

Conventional CO_2 sensors generally use Non-Dispersive Infrared (NDIR) technology.[8] Once there is moisture in the analyte gas or the CO_2 concentration is high, the absorption bands overlap and the CO_2 quantification is inaccurate. Photoacoustic CO_2 sensing is a mature technology,[9–11] but so far it has only been used in expensive laboratory-scale applications. Gravimetric sensors, like quartz crystal microbalance (QCM) sensors, have the advantages of simple device structure, high sensitivity, low cost, short analysis time and reusability.[12,13] The resonance frequency, which is proportional to the mass of the adsorbed molecules, is used as the sensor signal.[14] The affinity of the sensor can be tuned by modifying the QCM sensor

Karlsruhe Institute of Technology (KIT), Institute of Functional Interfaces (IFG), Hermann-von-Helmholtz-Platz 1, 76344 Eggenstein-Leopoldshafen, Germany. E-mail: Lars.Heinke@kit.edu

† Electronic supplementary information (ESI) available. See DOI: https://doi.org/10.1039/d2ta06324g

surface. For example, QCM-based sensors modified with nanoporous materials with large specific surface areas have been used for the detection of various gases and vapors.[15–18] QCM-based CO_2 sensors have been presented but, while the detection of large CO_2 concentrations is straightforward, the detection limit and sensitivity are, to date, too poor for practical applications.[19] The main challenge for gravimetric CO_2 sensors is the active sensing material which should have a high affinity towards CO_2, but a low affinity towards other gases, and CO_2 should adsorb reversibly allowing for repeatable sensor usage.

MOFs are a class of nanoporous materials, composed of metal nodes connected by organic ligand molecules.[20,21] The structure and properties of MOFs can be designed to a wide extent. In this way, the chemical building blocks, the pore size and shape, the surface functionality and even orderliness have been modified to optimize the CO_2 adsorption capacity.[22–26] However, for practical applications, the CO_2 affinity has to be significantly increased and the cross-sensitivity to other gases has to be generally decreased. Ionic liquids (ILs) are a class of unique liquids with high CO_2 affinities.[27,28] ILs are composed of organic cationic and anionic molecules and have a wide structural and functional diversity.[29–31] Based on their CO_2 affinity, ILs are used as active sensing materials for sensing CO_2.[32–34] However, their liquid and non-porous nature hamper their application in sensors.[35,36] Nanoporous MOF materials can serve as host materials for the embedment of ILs, and the combination of the two can enhance the CO_2 sensing performance.[37,38] IL@MOF composites were also used in various applications, for example, they show a strong performance in CO_2 adsorption[39–42] and separation,[43–46] I_2 capture,[47] heterogeneous catalysis[48–51] or battery applications.[52–54] For sensor applications, the cross-sensitivity, which means that the CO_2-concentration signal is interfered by the presence of humidity and other gas or vapor molecules, is often a severe issue, but unexplored to date. A powerful method to minimize the cross-sensitivity is to use arrays of sensors with different affinities. Such a sensor system is also referred to as electronic nose, e-nose.[55–57]

Here, we present a sensing system capable of detecting CO_2 and its mixtures with common vapor molecules. It is based on an electronic nose (e-nose), which is an array of QCM sensors coated with 2 different nanoporous MOF films, which are MOFs of type HKUST-1 and UiO-66, Fig. 1. (HKUST-1 stands for Hong Kong University of Science and Technology 1, also known as $Cu_3(BTC)_2$ with BTC = benzene-1,3,5-tricarboxylate), and UiO stands for Universitetet i Oslo.) To enhance the CO_2 affinity and selectivity, six sensors of each MOF structure were loaded with three different ionic liquids: [BMIM][SCN], [BMIM][TFSI], [BMIM][PF_6] with pore fillings of 20% and 50%. ([BMIM] stands for 1-butyl-3-methylimidazolium, [SCN] for thiocyanate, [TFSI] for bis(trifluoromethylsulfonyl)imide and [PF_6] for hexafluorophosphate). Higher IL-pore-fillings are avoided, due to the decreased free pore volume resulting in slow analyte diffusion and uptake. MOF films of type HKUST-1 and UiO-66 were chosen, because of: (1) their appropriate pore size, which is large enough to host ILs; (2) their pronounced stability, also when loaded with IL. Moreover, UiO-66 is also stable under humid conditions. (3) The syntheses of both MOFs were optimized allowing the preparation of homogeneous and highly crystalline films. The responses of the e-nose to different gases or vapors of CO_2, N_2, ethanol, methanol and water as well as some mixtures were tested. As expected, the sensor signal (or uptake) of most analyte molecules was reduced by the IL embedment in the MOF pores, due to the reduced free pore volume. On the other hand, the IL embedment results in an increased uptake of CO_2 and water upon IL-embedment, despite the reduced free pore volume. The ratio of the IL-embedment-caused signal increase for CO_2 varies with the MOF structure and the type of IL, resulting in different sensitivities of the different IL@MOF-sensors. With a neural network-based machine learning algorithm,[58] the data of the sensor array were analyzed. As a result, the e-nose can quantify the CO_2 concentration down to a limit of detection below the CO_2 level in air and can distinguish between the different gases and mixtures with 98% accuracy. This study shows that the ionic-liquid-loading in nanoporous materials can enhance the CO_2 sensitivity and selectivity and that such IL@MOF-based sensor arrays show superior performance for CO_2 sensing.

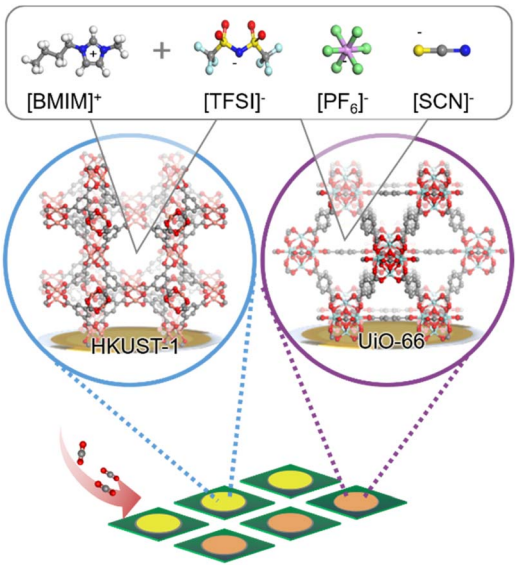

Fig. 1 Sketch of the MOF films, the IL structures and the sensor array. The MOF structures and the IL ions are labelled. The color code of the atoms is: C grey, H white (not shown for the MOFs), O red, N blue, Cu orange, Zr cyan, F green, N blue and S yellow. The ILs are [BMIM][TFSI], [BMIM][PF_6] and [BMIM][SCN].

Experimental section

MOF film syntheses

All MOF films are prepared on silver-coated QCM sensors. The HKUST-1 films were prepared using a layer-by-layer (lbl) method by sequentially exposing the substrate surface to the solutions of the metal nodes and of the linker molecules, resulting in surface-mounted MOFs (SURMOFs).[59,60] The MOF films with an HKUST-1 structure[61] were prepared from an ethanolic solution of 1 mM copper acetate and 0.2 mM BTC. The lbl SURMOF

synthesis was performed by the spray method[62] with 100 synthesis cycles. Prior to the SURMOF syntheses, all QCM substrates were functionalized with a 11-mercapto-1-undecanol (MUD) self-assembled monolayer (SAM).

UiO-66 films were prepared by the vapor-assisted conversion (VAC) method.[63] $ZrOCl_2$, terephthalic acid (BDC) and acetic acid were dissolved in DMF as the precursor solution. DMF and acetic acid mixture solution were filled in the glass vessel as a vapor source. One drop (50 μL) of the precursor solution was deposited uniformly on the sensor surface. The vessel was then sealed and heated to 120 °C for 3 hours. Finally, the samples were dried in vacuum at room temperature.

Embedment of IL in MOF films

The loading of the MOF films with IL was performed by immersing the samples in an IL/acetonitrile solution, as optimized in previous publications.[64–66] The immersion was carried out at room temperature for about 20 minutes. Afterwards, the sample was rinsed for about 2 seconds using acetonitrile and then dried in a stream of pure nitrogen. The IL concentration in acetonitrile was 20% and 50%, respectively, resulting in roughly 20% and 50% IL pore filling, respectively.[64–66] The sensor names with the MOF structures and the IL-loadings are given in Table 1.

Characterization of samples

X-ray diffraction (XRD). XRD analysis was performed using a Bruker D8 X-ray diffractometer. The X-ray optical path of the goniometer is in the Bragg–Brentano geometry (θ–θ). The X-ray wavelength is $\lambda = 0.154$ nm (CuKα).

Scanning electron microscopy (SEM). SEM images were taken with a TESCAN VEGA3 SEM. A thin (~5 nm) platinum film was sputtered onto the sample using a LEICA EM ACE600 high vacuum coater to avoid charge accumulation on the sample surface and to improve the image quality.

e-nose/sensor array. The electronic nose (e-nose) is a home-made multi-channel QCM sensor array, see Fig. 1 and S1.† Each sensor, which is an AT-cut quartz crystal, has a resonant frequency of 10 MHz. The QCM sensors are all purchased from JWT China, and their core components are circular quartz crystals of about 10 mm in diameter. The top and bottom surfaces of the resonant substrate are covered with circular Ag electrodes with a diameter of about 6 mm and an area of 28.3 mm^2. The MOF films were grown on the surfaces of the top Ag electrodes. In the experiment, the frequency shifts of all sensors were recorded every 1–1.7 seconds. The whole system was controlled by a program code written in MATLAB.

The gas flow system used to generate a specific content of the target analyte is shown in Fig. S1.† Argon is used as the carrier gas, while CO_2 and nitrogen are the analyte gases. Their flow rates are controlled by mass flow controllers. Different concentrations of CO_2 (or nitrogen) are realized by mixing the pure argon and CO_2 gas streams (or nitrogen stream). The mixing ratio of the two gas streams is controlled by mass flow controllers. For example, the flow rate in the argon channel is 196.06 ml min^{-1} and the CO_2 stream is 3.94 ml min^{-1}, resulting in a gas mixture with a CO_2 concentration of 1.97%$_{vol}$ (or 2 kPa). Methanol, ethanol and water enriched gas flows were prepared like in our previous publications.[67,68] One stream passes through the gas wash bottle and bubbles through the liquid VOC to produce VOC-enriched vapor. The other stream is pure argon. The two streams are then combined and the VOC concentration can be controlled by adjusting the flow rates.

Each sensing experiment consists of 3 phases. First, the sensor is in a pure argon gas stream and the MOF pores are emptied. This is the baseline. Then, the gas stream is instantaneously switched to the analyte-enriched argon gas with a constant analyte concentration. The adsorption of analyte molecules in the MOF film leads to an increase in mass and, thus, in a change in the frequency of the QCM sensor, which is the sensor signal. The third step is the desorption of the adsorbed molecules in pure argon gas. The adsorption step is 30 minutes long. The desorption step is typically 60 minutes long to ensure that all gas molecules are desorbed. In the

Table 1 The sensor names, the IL loading (determined by EDX, see Table S2) as well as the sensitivities and LODs of the individual sensors determined from Fig. 3

Sensor name	IL and MOF	IL loading in IL pairs per unit cell	Sensitivity in Hz/%$_{vol}$					LOD in %$_{vol}$				
			CO_2	N_2	Ethanol	Methanol	Water	CO_2	N_2	Ethanol	Methanol	Water
S1	HKUST-1 (empty)	0	47.041	17.077	141.2	190.64	95.941	0.0102	0.0281	0.0034	0.0025	0.005
S2	$[BMIM][TFSI]_{20\%}$ @HKUST-1	5.3 ± 1.4	47.657	13.109	118.4	164.61	136.72	0.0101	0.0336	0.0041	0.0029	0.0035
S3	$[BMIM][TFSI]_{50\%}$ @HKUST-1	9.8 ± 0.3	53.307	10.016	110.13	154.4	188.6	0.009	0.0479	0.0044	0.0031	0.0025
S4	$[BMIM][SCN]_{20\%}$ @HKUST-1	6.1 ± 1.1	51.116	14.213	128.42	169.45	170.8	0.0094	0.0338	0.0037	0.0028	0.0028
S5	$[BMIM][SCN]_{50\%}$ @HKUST-1	11.9 ± 0.4	56.174	10.937	110.74	161.2	212.68	0.0085	0.0439	0.0043	0.003	0.0023
S6	$[BMIM][PF_6]_{20\%}$ @HKUST-1	5.1 ± 1.6	47.026	13.276	117.98	164.15	149.4	0.0102	0.0362	0.0041	0.0029	0.0032
S7	$[BMIM][PF_6]_{20\%}$ @HKUST-1	9.7 ± 1.1	52.995	10.002	109.45	154.35	196.2	0.0091	0.048	0.0044	0.0031	0.0024
S8	UiO-66 (empty)	0	37.477	11.268	104.25	146.56	94.85	0.0128	0.0426	0.0046	0.0033	0.0051
S9	$[BMIM][TFSI]_{20\%}$ @UiO-66	1.7 ± 0.6	39.144	8.656	88.084	129.57	127.75	0.0123	0.0555	0.0054	0.0037	0.0038
S10	$[BMIM][TFSI]_{50\%}$ @UiO-66	5.5 ± 0.6	41.397	7.075	81.506	123.98	151.57	0.0116	0.0678	0.0059	0.0039	0.0032
S11	$[BMIM][SCN]_{20\%}$ @UiO-66	2.3 ± 0.6	40.108	9.664	93.637	133.48	136.25	0.012	0.0497	0.0051	0.0036	0.0035
S12	$[BMIM][SCN]_{50\%}$ @UiO-66	6.2 ± 0.9	44.157	7.67	83.631	126.62	192.68	0.0109	0.0626	0.0057	0.0038	0.0025
S13	$[BMIM][PF_6]_{20\%}$ @UiO-66	2.2 ± 0.9	38.983	8.63	87.545	129.12	141.99	0.0123	0.0556	0.0055	0.0037	0.0034
S14	$[BMIM][PF_6]_{50\%}$ @UiO-66	4.9 ± 0.6	41.127	7.058	81.062	123.72	155.17	0.0117	0.068	0.0059	0.0039	0.0031

experiments, 35 different analyte concentrations, see Table S1,† were used. All experiments were performed at room temperature (295 K).

Data analysis. For data analysis, a neural network written in python was used for classification and regression to determine the gas composition and content in the gas mixture.[69] The Pytorch[70] framework was used for the construction of the neural network and the qualitative and quantitative prediction of the gas mixture. The neural network consists of four hidden layers with 14 inputs per input layer, 128 neurons per hidden layer, 32 outputs per output layer for classification, and two outputs per output layer for the regression task. A linear rectification function[71] and a stochastic gradient descent optimizer[72] were used. For analyzing the sensor data, 100 data points were taken 120 s after the start of each gas molecule exposure period, see red arrows in Fig. 2. (Please note, data points taken later in the sensor experiments result in the same sensor performance, see Fig. 6 below.) From the resulting input data, classification was performed using 10-fold cross-validation, with 90% used as training data and 10% used as test data. A mean square error loss function[73] was used for the regression task. A cross-entropy loss function was used for the classification task. Thus, the composition and content of the gas mixture are simultaneously estimated by the neural network output. The program code is given in the ESI.†

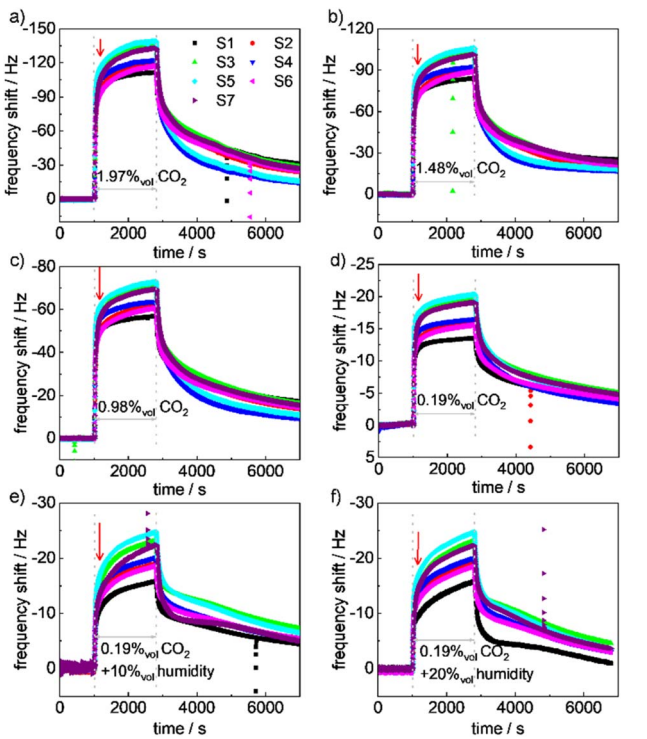

Fig. 2 E-nose data as a function of time. The signals are shown for the exposure to CO_2 with a concentration of 1.97%$_{vol}$ (a), 1.48%$_{vol}$ (b), 0.98%$_{vol}$ (c) and 0.19%$_{vol}$ (d) as well as 0.19% of CO_2 with 10% humidity (e) and 20% humidity (f), respectively. The gas concentrations are labelled in the panels. The color code for the MOF sensors is shown in the legend, the sample names are given in Table S1.† The red arrows indicate the data taken for the sensor performance analysis (Fig. 3–5).

Results and discussion

The entire e-nose, *i.e.*, the sensor array, is composed of 14 QCM sensors coated with HKUST-1 MOF films (7 times) and with UiO-66 MOF films (7 times). While one MOF film each remained empty (without IL-loading), 6 HKUST-1 films and 6 UiO-66 films were loaded with three different ionic liquids and 20% and 50% pore filling, respectively. The X-ray diffractograms of the samples (Fig. S2†) show that the MOF films are crystalline with the target HKUST-1 and UiO-66 structures. The diffractograms of the samples are very similar, indicating a very similar crystallinity of the samples. In addition, the diffraction patterns show that the crystal structures of all samples remain unchanged upon IL loading. The samples were further characterized by infrared and energy-dispersive X-ray (EDX) spectroscopy, Fig. S4 and S5,† verifying the targeted MOF structure and IL embedment. The amount of the IL content per MOF unit cell is quantified by EDX spectroscopy. The determined content is shown in Table 1 and S2†.

To explore the performance of the sensor array, gas sensing experiments were conducted for different concentrations of CO_2, N_2, ethanol, methanol and H_2O. Argon was chosen as the carrier gas because of the small interaction between the noble gas and the nanoporous host, resulting in a very small argon uptake at room temperature. When the gas flow through the e-nose was switched from initially pure argon to the analyte-enriched argon flow, the frequency shifts of all QCM sensors changed, which are proportional to the mass of the adsorbed analyte molecules in the MOF films. The frequency shifts were recorded as sensing signals. In this way, the response of the sensor array was explored for different compositions and different concentrations of gas mixtures, *i.e.*, CO_2 (0.09–1.97%$_{vol}$), N_2 (0.09–1.97%$_{vol}$), ethanol (0.09–1.97%$_{vol}$), methanol (0.09–1.97%$_{vol}$) and water vapor (0.09%$_{vol}$ and 0.19%$_{vol}$). In addition, the response of the sensor array to $CO_2 : N_2 = 1 : 1$ gas mixtures (2%$_{vol}$ and 0.09%$_{vol}$ in argon) and to 0.19%$_{vol}$ CO_2 with different humidity levels (10%, 20% and 30%, which correspond to concentrations of 0.23%$_{vol}$, 0.46%$_{vol}$ and 0.68%$_{vol}$) was also explored. In total, 35 experiments with different concentrations and compositions were performed, see Table S1.† Fig. 2 shows the frequency shift of the HKUST-1 QCM sensor array when exposed to CO_2 at different concentrations. Further adsorption data are shown in Fig. S6–S18.† All transient uptake (*i.e.*, analyte exposure) and release curves are qualitatively similar.

All sensor signals as a function of different concentrations of CO_2, N_2, ethanol, methanol and water are shown in Fig. 3 for the HKUST-1 sensors (sensors S1–S7) and in Fig. S20 and S21† for the UiO-66 sensors (sensors S8–S14).

The data for all sensors and gas molecules are essentially linear and can be described with the Henry's region of a Langmuir isotherm. Fig. 3f shows the ratios of the CO_2 and N_2 uptake of an individual IL-loaded sensor relative to the CO_2 and N_2 uptake by the empty HKUST-1 sensor. The relative values of ethanol, methanol and water uptake are shown in Fig. S19.† As shown, there is a significant difference in the adsorption of CO_2

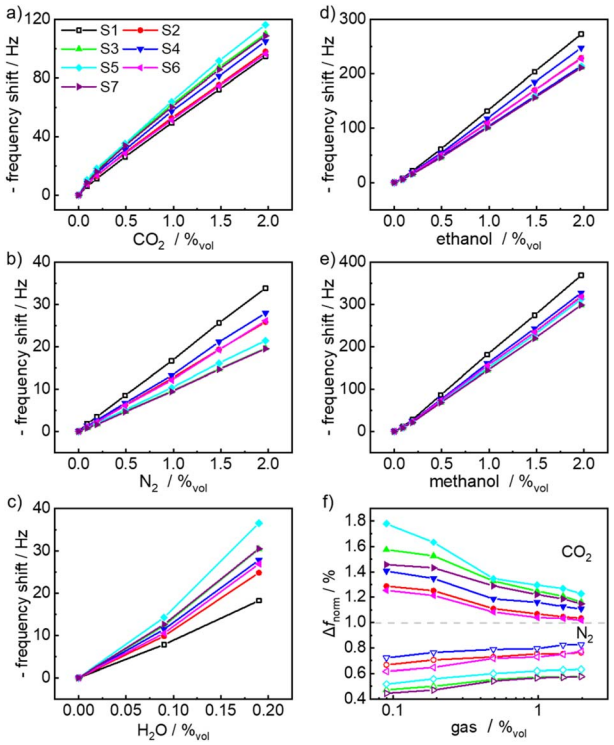

Fig. 3 Negative values of the frequency shift *versus* gas concentration of (a) CO_2, (b) N_2, (c) H_2O, (d) ethanol and (e) methanol. For all HKUST-1 MOF sensors, the frequency shift (which is proportional to the mass change) exhibits an essentially linear dependence on the gas concentration in the explored range. (f) Ratio (Δf_{norm}) of the gas uptake by the sensors loaded with IL and the gas uptake by the empty HKUST-1 sensor *versus* the gas concentration.

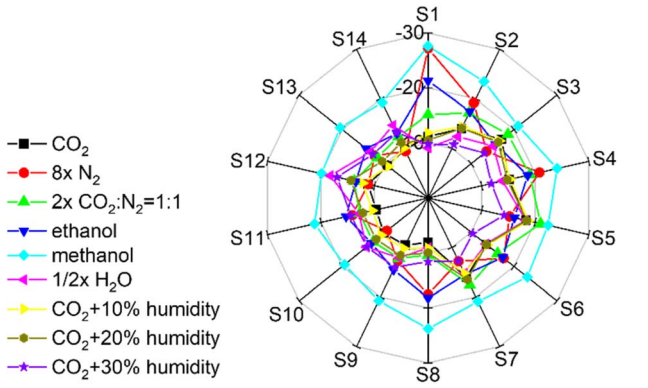

Fig. 4 Radar plot of the frequency shift Δf for exposure to gases of 0.19%$_{vol}$ concentration. The gases are CO_2, N_2, $CO_2:N_2 = 1:1$, ethanol, methanol, H_2O, CO_2 + 10%, 20% and 30% humidity, respectively, see labels. Each axis (with a scale from 0 to 30 Hz) represents a different sensor, see Table 1. For better visibility, the data of nitrogen have been multiplied by 8, of $CO_2:N_2 = 1:1$ mixture by 2 and the H_2O data have been divided by 2.

and water *versus* N_2, ethanol and methanol by the IL-loaded sensors. The IL-embedment results in a smaller uptake of nitrogen, ethanol and methanol. This is caused by the IL in the pores, reducing the available pore volume of the MOF. On the other hand, the uptakes of water and CO_2 increase for the IL-loaded sensors compared to the empty-MOF sensors. For example, the uptake of CO_2 by HKUST1 loaded with 50% pore filling of [BMIM][SCN] increased by 69%, compared to the empty MOF sensor. This is due to the stronger solubilization ability of the ionic liquid for CO_2 (and water).[74] Although CO_2 is a non-polar molecule, it has a large quadruple dipole moment and polarizability, which account for its strong interaction with the IL molecules. The interaction between the CO_2 molecules and the IL molecules in the pore is based on the electrostatic interaction between the ionic liquid and CO_2.[75,76] In addition, weak dispersive interaction may contribute to the energy.[76] It was found that the interaction between CO_2 and the IL, and thus the solubility, is dominated by the anions, rather than the cations.[75] In line with solubility studies of different (bulk) ILs based on BMIM,[75] the interaction of CO_2 with TFSI is larger than that with PF_6, see Fig. 3f or Table 1.

The slopes of the linear range of the isotherm, which correspond to the sensitivity, are shown in Table 1. It is worth noting that each sensor has a different slope for the same gas molecule. This is caused by the fact that the MOF material is loaded with different concentrations and different types of ILs. For CO_2, the [BMIM][SCN]$_{50\%}$@HKUST-1 sensor showed the largest sensitivity, followed by the [BMIM][TFSI]$_{50\%}$ @HKUST-1. More importantly, the same sensor showed different sensitivities for different analytes. For the HKUST-1 sensors, the CO_2 sensitivity ranges between 47.0 Hz/%$_{vol}$ for the empty MOF (S1) and 56.2 Hz/%$_{vol}$ for the MOF with 50% pore filling of [BMIM][SCN] (S5). The sensitivities of the HKUST-1 sensors for N_2, ethanol, methanol and water are in the ranges of 10–17 Hz/%$_{vol}$, 109–141 Hz/%$_{vol}$, 154–191 Hz/%$_{vol}$ and 95–213 Hz/%$_{vol}$, respectively. For UiO-66, the CO_2 sensitivity ranges between 37.5 Hz/%$_{vol}$ for the empty MOF (S8) and 44.2 Hz/%$_{vol}$ for the MOF with 50% pore filling of [BMIM][SCN] (S12). The sensitivities of the UiO-66 sensors for N_2, ethanol, methanol and water are in the ranges of 7.0–11.3 Hz/%$_{vol}$, 81–104 Hz/%$_{vol}$, 124–147 Hz/%$_{vol}$ and 95–193 Hz/%$_{vol}$, respectively. Most importantly, the different combinations of IL and MOF structures result in different sensitivities for each analyte. This feature is important for distinguishing the analytes *via* machine learning, see below (and see also Fig. 4 below).

The limits of detection (LODs, Table 1) of individual sensors are calculated as 3 times the standard deviation divided by the sensitivity. As standard deviation, we used the average value of the standard deviation of each individual sensor, determined from the baselines in Fig. 2 and S6–S9† before the analyte exposure begins (at about 1000 s). The average value of the standard deviation is 0.16 Hz. For the HKUST-1, while the empty sample (without IL) has a CO_2 LOD of 0.0102%$_{vol}$, the LODs of the IL@MOF sensors are significantly smaller, with the smallest LOD of only 0.0085%$_{vol}$ (*i.e.*, 85 ppm). This is lower than the present atmospheric CO_2 concentration of about 350 ppm (*i.e.* 0.035%$_{vol}$). The sensor arrays also have very low detection limits for N_2, ethanol and methanol, ranging from 0.0025 to 0.068%$_{vol}$.

In addition to exploring the sensor response to different concentrations of CO_2 and different concentrations of N_2, the sensor performance for different concentrations of CO_2–N_2 and

CO_2–water mixtures (in argon) was also experimentally explored. In Fig. S10 and S11,† the sensor array signal data *versus* time for different concentrations of CO_2 and N_2 gas mixtures are shown. The application of the sensor array in humid environments was also investigated. The response of the sensor array to 0.19%$_{vol}$ CO_2 with 10%$_{vol}$, 20%$_{vol}$ and 30%$_{vol}$ humidity was tested, Fig. S17 and S18.† Due to the high stability of UiO-MOFs[77] and due to the reproducibility of the uptake by UiO-66 in a moist atmosphere,[78] the UiO-66 sensor performance is not hampered by the humidity and the sensor can operate normally at 30%$_{vol}$ humidity. On the other hand, the HKUST-1 sensor exhibits a decrease in sensor signal at 30%$_{vol}$ humidity (compare Fig. 2e and f and S17†), which is attributed to the water-induced formation of defects in HKUST-1, decreasing the analyte uptake.[79] This means, while the IL@UiO-sensors are suitable for practical applications, also in a humid environment, the application of the IL@HKUST-1 is limited to a dry atmosphere.

Fig. 4 shows the radar plots of the frequency shift of the sensor array for a gas concentration of 0.19%$_{vol}$. Radar plots for different gas concentrations are shown in Fig. S23.† The radar plots show that each analyte has a unique response pattern that can be distinguished visually. This means that the sensor array can qualitatively distinguish between the gas molecules.

To quantitatively analyze the sensor performance for the different gas molecules, the sensor array data were analyzed with a machine learning algorithm, here a neural network was used. The confusion matrix visually reflects the classification performance of the algorithm, where the correct classification is on the diagonal. For a given analyte concentration, the confusion matrixes for CO_2, N_2, ethanol, methanol and $CO_2 : N_2 = 1 : 1$ are shown in Fig. S24.† It shows that the sensor array can accurately discriminate the analytes.

Typically, the components, composition and concentration of the analytes are unknown in a real-life sensing problem. Fig. S25† shows the confusion matrix for all the sensor data explored for different compositions and different concentrations of gases, from 0.09%$_{vol}$ content to 1.97%$_{vol}$ content. Their average classification accuracy is 93.8%.

The results of the sensor performance with the neural-network algorithm using only the data from some sensors (*i.e.* only a part of the sensor array) as input data are shown in Fig. 5. There, the input data are either only from the two empty MOF sensors, two IL-loaded-MOF sensors, two water-stable IL-loaded-UiO sensors and the entire sensor array. All analytes regardless of the concentration are individual classes. It shows that the full sensor array applied to all data without assigned

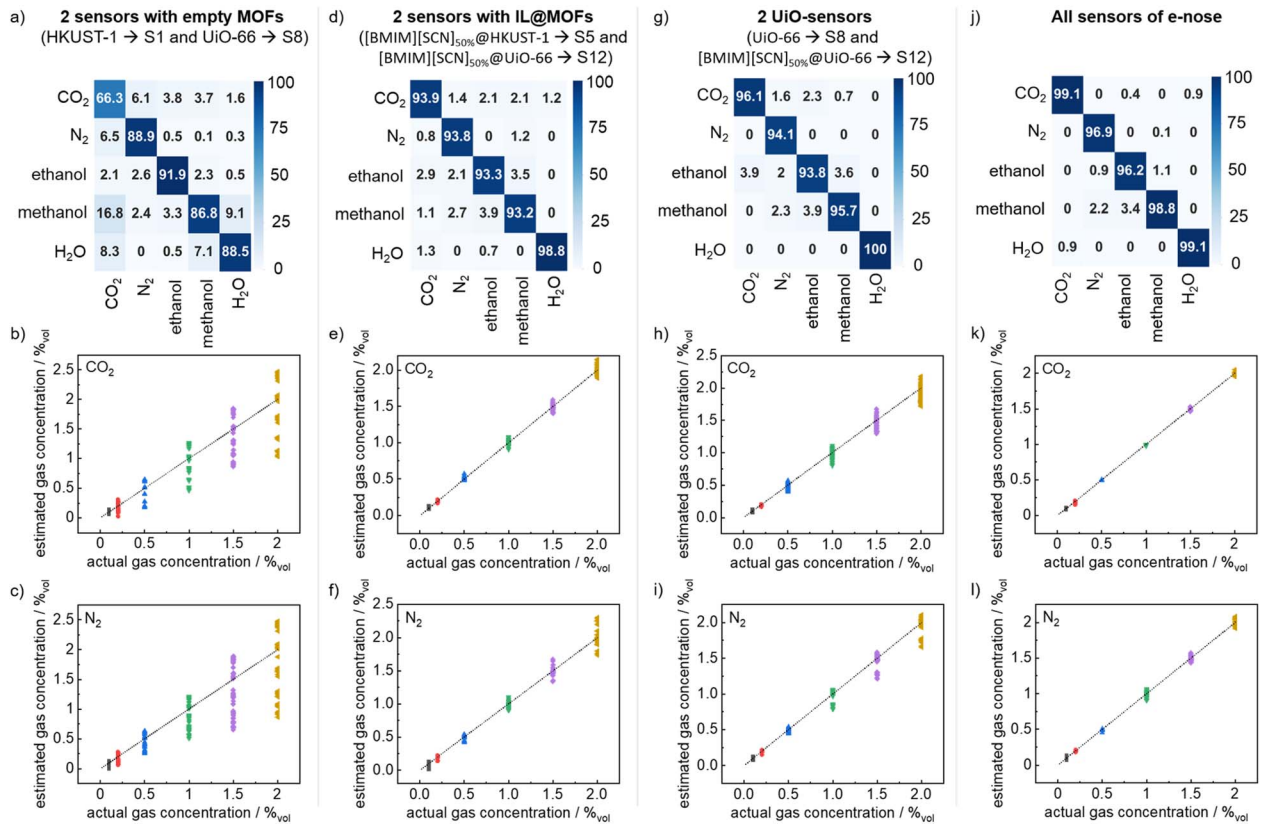

Fig. 5 The confusion matrixes and the comparison of actual gas concentrations with the estimated gas concentrations, as a result of the sensor data analysis with the neural-network algorithm. (a–c) The input data are from sensors S1 and S8, *i.e.* HKUST-1 and UiO-66 without IL-loading. (d–f) The input data are from sensors S5 and S12, *i.e.* [BMIM][SCN]$_{50\%}$@HKUST-1 and [BMIM][SCN]$_{50\%}$@UiO-66. (g–i) The input data are from two UiO-sensors (S8 and S12), *i.e.* UiO-66 and [BMIM][SCN]$_{50\%}$@UiO-66. (j–l) The input data comprise the data from all sensors (S1–S14). All concentrations of all CO_2, N_2, ethanol, methanol and $CO_2 : N_2 = 1 : 1$ are classified as one analyte each. (It corresponds to Fig. S25,† however, ignoring the gas concentration).

concentrations (*i.e.* classification of CO_2, N_2, ethanol, methanol and $CO_2:N_2 = 1:1$ without concentration information markers) achieves an outstanding classification accuracy of 98.0% (Fig. 5j). It shows that the IL@MOF-e-nose is fully capable of analyzing the gases (and mixtures) with unknown concentrations. For comparison, the data from only two sensors (S1 and S8) of plain MOF, *i.e.*, HKUST-1 and UiO-66 without IL loading, cannot clearly distinguish CO_2 from the other analytes, (Fig. 5a). The average accuracy is 84.5%, but only 66.3% for CO_2, which is unacceptable for practical applications.

On the other hand, two sensors of MOF (one HKUST-1 and one UiO-66) with embedded IL (*i.e.* $[BMIM][SCN]_{50\%}$ @HKUST-1, S5 and $[BMIM][SCN]_{50\%}$ @UiO-66, S12) can distinguish all analytes with an average accuracy of 94.6%, and can identify CO_2 with 93.9% accuracy (Fig. 5d).

For using only two water-stable UiO-MOFs, empty (S8) and filled with $[BMIM][SCN]_{50\%}$ (S12), the average classification accuracy is even slightly higher, 95.9% (Fig. 5g). This shows that 2 UiO-MOF-sensors filled with IL can be an excellent e-nose.

Based on the neural network, the quantitative analysis of different gas concentrations can be achieved by regressing a mixture of gases of different compositions using the sensor data not used in the training network, see Fig. 5 b, c, e, f, h, g, k and l. Using the data of the entire sensor array, the estimated concentration essentially agrees with the real CO_2 concentration with an average error of 2.7%.

The average error in estimating the N_2 concentration is 3.2%. The IL@MOF-e-nose not only has superb sensitivity and selectivity for a single target gas, but also can accurately predict the type and concentration of the gases. However, the regression task using only two sensors (S1 and S8) without IL-loading does not allow the quantitative analysis of the different gas concentrations, see Fig. 5b and c. The average error in the predicted CO_2 concentration is 37.5% and the average error in the predicted N_2 concentration reaches 39%.

For two IL-loaded sensors with high sensitivities (S5 and S12, Fig. 5e and f), the average errors for predicting the CO_2 and N_2 concentrations are 9.1% and 10.7%, respectively. For using only 2 water-stable UiO-MOFs (S8 and S12,† Fig. 5h and i), the average error for predicting the CO_2 and N_2 concentrations are 9.3% and 10.4%, respectively. The error in predicting the gas concentration is relatively small, so the sensor array enables effective prediction of the type and concentration of the target gas, especially CO_2.

The effect of ambient humidity on the sensor operation is explored in Fig. S26.† The entire sensor arrays can operate normally at humidity levels below 30%. When the humidity is 10% and 20%, the average error of the estimated CO_2 concentration is 5.2%. The average error in the estimated CO_2 concentration is 9.8% when the humidity is 30%. Using only the data of the UiO-sensors as the input (S8–S14), which are stable in humid environments, the average error in the estimated CO_2 concentration is 5.5%. For using only the data from 2 UiO-sensors, the average error in the estimated CO_2 concentration is still rather small, only 6.2%. This demonstrates the great performance of the e-nose under humid conditions.

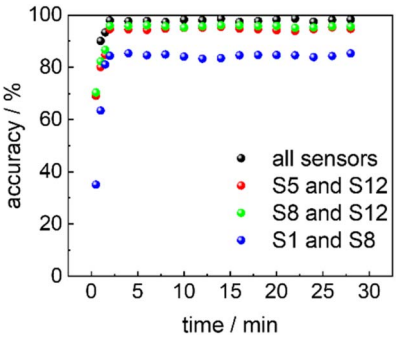

Fig. 6 Discrimination accuracy of 5 analytes (see Fig. 5a, d, g and j) at different time intervals. Each value is determined from 100 consecutive data points, corresponding to approximately 2 minute time intervals, where the final data points end at the values on the *x*-axis. The input data comprise data from the entire sensor array (black), the data for sensors S5 and S12 (red) and the data from sensors S1 and S8 (green). The *x*-axis is the time after the start of exposure to the analytes.

The transient signal of the sensor array can be described with a mono-exponential decay function with time constants of 0.6 to 2.0 min for the CO_2 uptake and roughly 6 min for the CO_2 release, see Table S3.† Based on the time constants, the sensor response time and recovery time can be calculated. On the other hand, although the signals have not yet reached its equilibrium values in the analyte atmosphere, the (non-equilibrium) data of the e-nose can be used for discriminating the analytes. The accuracy of discrimination of the sensor data as a function of time is shown in Fig. 6. The data show that the sensor array reaches its final classification accuracy about 2 minutes after start of the analyte exposure. This means, although the sensor response time has not yet passed, the sensor array is able to classify the analytes precisely.

The reproducibility of the data was explored by repeating the same analyte exposure experiments 4 times, see Fig. S27 and S28.† The data show that the signal is reproducible with only very small deviations between the different experiments. The average standard deviations between the signal were approximately 0.5 Hz, which is much smaller than the signal magnitude (of about 100 Hz).

While the experiments here were performed at room temperature, the QCM transducer also allows the sensing at other temperatures. With the knowledge of the adsorption enthalpy of the analytes in the IL@MOF material, the sensor response at different temperatures can be predicted. While the small changes of the resonance frequency occur when strongly changing the gas flow rate through the sensor cell, the sensor response is not affected by changes of the flow rate. The QCM sensors can be reused for preparing new IL@MOF films, after removing the MOF films from the surface (*e.g.*, by ultrasonication in water or aqueous acidic acid).

Conclusions

A gravimetric sensor array based on 14 QCM sensors coated with HKUST-1 and UiO-66 MOF films loaded with three different ionic

liquids, [BMIM][SCN], [BMIM][TFSI] and [BMIM][PF_6], at 20% and 50% concentrations is presented. The investigation of sensor response to different gases and vapor analytes, including CO_2, N_2, ethanol, methanol, water and some mixtures as well as simultaneous classification and regression based on neural-network machine learning analysis for different concentrations were performed. The data show that, in addition to an increase in sensitivity, the embedment of IL in the pores of MOFs enhances the selectivity significantly, especially with respect to CO_2. The presented IL@MOF-e-nose has a very low limit of detection of $0.0085\%_{vol}$ for CO_2 and excellent selectivity. Moreover, the e-nose was also able to predict the concentrations of the analytes with a very small error rate in the range of a few percent. By using only robust MOFs (*i.e.* UiO-66) as the IL-host, the sensor array also shows excellent performance in a humid environment, showing its potential for practical real-life applications.

Considering the huge variety of ionic liquids and nanoporous materials like MOFs, there exist endless possibilities of combining them and optimizing the selectivities. Thus, we believe there is large potential for sensors with nanoporous materials with enhanced sensitivities obtained by ionic-liquid embedment. We like to stress that the performance of the e-nose strongly depends on the used sensor, and picking the best sensors from a large selection is not a trivial task, see for instance (ref. 80 and 81). Therefore, we assume that the e-nose performance can be further enhanced by optimizing the sensor selection as well by optimizing the combinations of the MOF and IL.

Author contributions

PQ performed all experiments, supported by SO. YJ recorded the SEM images. PQ and LH wrote the manuscript, approved by all authors.

Conflicts of interest

There are no conflicts to declare.

Acknowledgements

We acknowledge funding through the China Scholarship Council (CSC) and the Deutsche Forschungsgemeinschaft (DFG, German Research Foundation, DFG HE 7036/5).

Notes and references

1 J. Rogelj, A. Popp, K. V. Calvin, G. Luderer, J. Emmerling, D. Gernaat, S. Fujimori, J. Strefler, T. Hasegawa, G. Marangoni, V. Krey, E. Kriegler, K. Riahi, D. P. van Vuuren, J. Doelman, L. Drouet, J. Edmonds, O. Fricko, M. Harmsen, P. Havlík, F. Humpenöder, E. Stehfest and M. Tavoni, *Nat. Clim. Change*, 2018, **8**, 325–332.

2 K. Permentier, S. Vercammen, S. Soetaert and C. Schellemans, *Int J Emerg Med.*, 2017, **10**, 14.

3 H. R. Ludwig, S. G. Carirelli and J. J. Whalen, *Documentation for Immediately Dangerous to Life or Health Concentrations (IDLHs)*, National Institute for Occupational Safety and Health (NIOSH), 1994, p. 82.

4 A. Lohila, T. Laurila, J.-P. Tuovinen, J. H. Mika Aurela, M. P. Tea Thum, J. Rinne and T. Vesala, *Environ. Sci. Technol.*, 2007, **41**, 2717–2722.

5 S. A. Prior, G. B. Runion, S. C. Marble, H. H. Rogers, C. H. Gilliam and H. A. Torbert, *HortScience*, 2011, **46**, 158–162.

6 S. Neethirajan, D. S. Jayas and S. Sadistap, *Food Bioprocess Technol.*, 2008, **2**, 115–121.

7 M. Ahila, J. Dhanalakshmi, J. C. Selvakumari and D. P. Padiyan, *Mater. Res. Express*, 2016, **3**, 105025.

8 X. Tan, H. Zhang, J. Li, H. Wan, Q. Guo, H. Zhu, H. Liu and F. Yi, *Nat. Commun.*, 2020, **11**, 5245.

9 H. S. M. d. Vries, M. A. J. Wasono, F. J. M. Harren, E. J. Woltering, H. C. P. M. v. d. Valk and J. Reuss, *Postharvest Biol. Technol.*, 1996, **8**, 1–10.

10 C. G. Teodoro, D. U. Schramm, M. S. Sthel, G. R. Lima, M. V. Rocha, J. R. Tavares and H. Vargas, *Infrared Phys. Technol.*, 2010, **53**, 151–155.

11 T. Yang, W. Chen and P. Wang, *Appl. Spectrosc. Rev.*, 2020, **56**, 143–170.

12 S. K. Vashist and P. Vashist, *J. Sens.*, 2011, **2011**, 1–13.

13 H.-H. Lu, Y. K. Rao, T.-Z. Wu and Y.-M. Tzeng, *Sens. Actuators, B*, 2009, **137**, 741–746.

14 G. Sauerbrey, *Zeitschrift fiir Physik*, 1959, **155**, 206–222.

15 N. L. Torad, S. Zhang, W. A. Amer, M. M. Ayad, M. Kim, J. Kim, B. Ding, X. Zhang, T. Kimura and Y. Yamauchi, *Adv. Mater. Interfaces*, 2019, **6**, 1900849.

16 E. Haghighi and S. Zeinali, *Microporous Mesoporous Mater.*, 2020, **300**, 110065.

17 L. Wang, *Sens. Actuators, A*, 2020, **307**, 111984.

18 S. Okur, P. Qin, A. Chandresh, C. Li, Z. Zhang, U. Lemmer and L. Heinke, *Angew. Chem., Int. Ed. Engl.*, 2021, **60**, 3566–3571.

19 J. Devkota, K. J. Kim, P. R. Ohodnicki, J. T. Culp, D. W. Greve and J. W. Lekse, *Nanoscale*, 2018, **10**, 8075–8087.

20 O. M. Yaghi, M. J. Kalmutzki and C. S. Diercks, *Introduction to Reticular Chemistry: Metal-Organic Frameworks and Covalent Organic Frameworks*, Wiley, 2019, p. 552, ISBN: 978-3-527-34502-1.

21 S. Kaskel, *The Chemistry of Metal-Organic Frameworks: Synthesis, Characterization, and Applications*, Wiley, 2016, P. 904, ISBN: 978-3-527-33874-0.

22 J. An and N. L. Rosi, *J. Am. Chem. Soc.*, 2010, **132**, 5578–5579.

23 L. Valenzano, B. Civalleri, S. Chavan, G. T. Palomino, C. O. Areán and S. Bordiga, *J. Phys. Chem. C*, 2010, **114**, 11185–11191.

24 H.-Y. Cho, D.-A. Yang, J. Kim, S.-Y. Jeong and W.-S. Ahn, *Catal. Today*, 2012, **185**, 35–40.

25 S. Choi, T. Watanabe, T. H. Bae, D. S. Sholl and C. W. Jones, *J. Phys. Chem. Lett.*, 2012, **3**, 1136–1141.

26 T. Ghanbari, F. Abnisa and W. M. A. Wan Daud, *Sci. Total Environ.*, 2020, **707**, 135090.

27 J. L. Anderson, J. K. Dixon and J. F. Brennecke, *Acc. Chem. Res.*, 2007, **40**, 1208–1216.

28 M. J. Muldoon, S. N. V. K. Aki, J. L. Anderson, J. K. Dixon and J. F. Brennecke, *J. Phys. Chem. B*, 2007, 9001–9009.

29 H. Weingartner, *Angew. Chem., Int. Ed. Engl.*, 2008, **47**, 654–670.
30 J. D. Holbrey and K. R. Seddon, *Clean Prod. Process.*, 1999, **1**, 223–236.
31 R. D. Rogers and K. R. Seddon, *Science*, 2003, **302**, 792–793.
32 D. S. Silvester, *Analyst*, 2011, **136**, 4871–4882.
33 D. Wei and A. Ivaska, *Anal. Chim. Acta*, 2008, **607**, 126–135.
34 K. P. S. Hussan, H. H. Moidu, M. S. Thayyil, T. V. Jinitha, A. Antony and G. Govindaraj, *J. Mater. Sci.: Mater. Electron.*, 2021, **32**, 25164–25174.
35 R. V. Barrulas, M. Zanatta, T. Casimiro and M. C. Corvo, *Chem. Eng. J.*, 2021, **411**, 128528.
36 S. Zhang, K. Dokko and M. Watanabe, *Mater. Horiz.*, 2015, **2**, 168–197.
37 M. Mohamedali, A. Henni and H. Ibrahim, *Microporous Mesoporous Mater.*, 2019, **284**, 98–110.
38 W. Chen, Z. Zhang, C. Yang, J. Liu, H. Shen, K. Yang and Z. Wang, *J. Membr. Sci.*, 2021, **636**, 119581.
39 A. Aijaz, T. Akita, H. Yang and Q. Xu, *Chem. Commun.*, 2014, **50**, 6498–6501.
40 Z. Bian, X. Zhu, T. Jin, J. Gao, J. Hu and H. Liu, *Microporous Mesoporous Mater.*, 2014, **200**, 159–164.
41 C. Chen, N. Feng, Q. Guo, Z. Li, X. Li, J. Ding, L. Wang, H. Wan and G. Guan, *J. Colloid Interface Sci.*, 2018, **521**, 91–101.
42 J. M. Vicent-Luna, J. J. Gutierrez-Sevillano, S. Hamad, J. Anta and S. Calero, *ACS Appl. Mater. Interfaces*, 2018, **10**, 29694–29704.
43 J. Ma, Y. Ying, X. Guo, H. Huang, D. Liu and C. Zhong, *J. Mater. Chem. A*, 2016, **4**, 7281–7288.
44 M. Zeeshan, V. Nozari, M. B. Yagci, T. Isik, U. Unal, V. Ortalan, S. Keskin and A. Uzun, *J. Am. Chem. Soc.*, 2018, **140**, 10113–10116.
45 H. M. Polat, M. Zeeshan, A. Uzun and S. Keskin, *Chem. Eng. J.*, 2019, **373**, 1179–1189.
46 W. Chen, Z. Zhang, C. Yang, J. Liu, H. Shen, K. Yang and Z. Wang, *J. Membr. Sci.*, 2021, **636**, 119581.
47 Y. Tang, H. Huang, J. Li, W. Xue and C. Zhong, *J. Mater. Chem. A*, 2019, **7**, 18324–18329.
48 Q.-x. Luo, X.-d. Song, M. Ji, S.-E. Park, C. Hao and Y.-q. Li, *Appl. Catal., A*, 2014, **478**, 81–90.
49 S. Abednatanzi, A. Abbasi and M. Masteri-Farahani, *Catal. Commun.*, 2017, **96**, 6–10.
50 S. Abednatanzi, K. Leus, P. G. Derakhshandeh, F. Nahra, K. De Keukeleere, K. Van Hecke, I. Van Driessche, A. Abbasi, S. P. Nolan and P. V. Der Voort, *Catal. Sci. Technol.*, 2017, **7**, 1478–1487.
51 H. M. A. Hassan, M. A. Betiha, S. K. Mohamed, E. A. El-Sharkawy and E. A. Ahmed, *J. Mol. Liq.*, 2017, **236**, 385–394.
52 Z. Wang, R. Tan, H. Wang, L. Yang, J. Hu, H. Chen and F. Pan, *Adv. Mater.*, 2018, 30.
53 T. Chen, S. Chen, Y. Chen, M. Zhao, D. Losic and S. Zhang, *Mater. Chem. Front.*, 2021, **5**, 1771–1794.
54 Z.-J. Zheng, H. Ye and Z.-P. Guo, *Energy Environ. Sci.*, 2021, **14**, 1835–1853.
55 C. Gonzalez Viejo, S. Fuentes, A. Godbole, B. Widdicombe and R. R. Unnithan, *Sens. Actuators, B*, 2020, **308**, 127688.
56 M. Taştan and H. Gökozan, *Appl. Sci.*, 2019, **9**, 3435.
57 S. Esfahani, A. Tiele, S. O. Agbroko and J. A. Covington, *Sensors (Basel)*, 2020, **20**, 6875.
58 H. A. Rowley, S. Member, S. Baluja and T. Kanade, *IEEE Trans. Pattern Anal. Mach. Intell.*, 1998, **20**, 23–28.
59 O. Shekhah, H. Wang, D. Zacher, R. A. Fischer and C. Wöll, *Angew. Chem., Int. Ed. Engl.*, 2009, **48**, 5038–5041.
60 L. Heinke and C. Wöll, *Adv. Mater.*, 2019, **31**, e1806324.
61 S. S.-Y. Chui, S. M.-F. Lo, J. P. H. Charmant, A. G. Orpen and I. D. Williams, *Science*, 1999, **283**, 1148–1150.
62 S. Hurrle, S. Friebe, J. Wohlgemuth, C. Wöll, J. Caro and L. Heinke, *Chem.–Eur. J.*, 2017, **23**, 2294–2298.
63 E. Virmani, J. M. Rotter, A. Mahringer, T. von Zons, A. Godt, T. Bein, S. Wuttke and D. D. Medina, *J. Am. Chem. Soc.*, 2018, **140**, 4812–4819.
64 A. B. Kanj, R. Verma, M. Liu, J. Helfferich, W. Wenzel and L. Heinke, *Nano Lett.*, 2019, **19**, 2114–2120.
65 M. Vazquez, M. Liu, Z. Zhang, A. Chandresh, A. B. Kanj, W. Wenzel and L. Heinke, *ACS Appl. Mater. Interfaces*, 2021, **13**, 21166–21174.
66 Z. Zhang, C. Li, A. Chandresh and L. Heinke, *Ionics*, 2021, 487–494, DOI: **10.1007/s11581-021-04249-w**.
67 P. Qin, B. A. Day, S. Okur, C. Li, A. Chandresh, C. E. Wilmer and L. Heinke, *ACS Sens.*, 2022, **7**, 1666–1675.
68 P. Qin, S. Okur, C. Li, A. Chandresh, D. Mutruc, S. Hecht and L. Heinke, *Chem. Sci.*, 2021, **12**, 15700–15709.
69 M. Barriault, I. Alexander, N. Tasnim, A. O'Brien, H. Najjaran and M. Hoorfar, *Sens. Actuators, B*, 2021, **326**, 129012.
70 S. C. van de Leemput, J. Teuwen, B. van Ginneken and R. Manniesing, *J. Open Res. Softw.*, 2019, **4**, 1576.
71 A. L. Maas, A. Y. Hannun and A. Y. Ng, *Proc. Int. Conf. Mach. Learn.*, 2013, **30**, 3.
72 A. A. Lydia and F. S. Francis, *Int. J. Inf. Comput. Sci*, 2019, **6**, 566–568.
73 D. Harvey, S. Leybourne and P. Newbold, *Int. J. Forecast.*, 1997, **13**, 281–291.
74 C. Cadena, J. L. Anthony, J. K. Shah, T. I. Morrow, J. F. Brennecke and E. J. Maginn, *J. Am. Chem. Soc.*, 2004, **126**, 5300–5308.
75 S. J. Zeng, X. Zhang, L. P. Bai, X. C. Zhang, H. Wang, J. J. Wang, D. Bao, M. D. Li, X. Y. Liu and S. J. Zhang, *Chem. Rev.*, 2017, **117**, 9625–9673.
76 H. Weingaertner, *Angew. Chem., Int. Ed.*, 2008, **47**, 654–670.
77 N. C. Burtch, H. Jasuja and K. S. Walton, *Chem. Rev.*, 2014, **114**, 10575–10612.
78 C. Li, A. Chandresh, Z. Zhang, S. Moulai and L. Heinke, *Adv. Mater. Interfaces*, 2022, **9**, 2101947.
79 L. Heinke, Z. Gu and C. Wöll, *Nat. Commun.*, 2014, **5**, 4562.
80 J. A. Gustafson and C. E. Wilmer, *J. Phys. Chem. C*, 2017, **121**, 6033–6038.
81 J. A. Gustafson and C. E. Wilmer, *ACS Sens.*, 2019, **4**, 1586–1593.